

Thermo-optical spiking and mixed-mode oscillations in injected Kerr microcavities

Elias R. Koch,^{1,*} Julien Javaloyes,² and Svetlana V. Gurevich^{1,3}

¹*Institute for Theoretical Physics, University of Münster,
Wilhelm-Klemm-Str. 9, 48149 Münster, Germany*

²*Departament de Física, Universitat de les Illes Balears & IAC-3,
Cra. de Valldemossa, km 7.5, E-07122 Palma de Mallorca, Spain*

³*Center for Nonlinear Science (CeNoS), University of Münster, Corrensstraße 2, 48149 Münster, Germany*

(Dated: December 4, 2024)

We investigate the nonlinear dynamics of vertically emitting Kerr microcavities under detuned optical injection, considering the impact of slow thermal effects. Our model integrates thermal detuning caused by refractive index shifts due to heating. Through numerical and analytical approaches, we uncover a rich spectrum of dynamical behaviors, including excitable thermo-optical pulses, mixed-mode oscillations, and chaotic spiking, governed by a higher-dimensional canard scenario. Introducing a long external feedback loop with time delays comparable to the microcavity photon lifetime but shorter than thermal relaxation timescales, reveals how delay affects excitability and stabilizes temporal localized states. Our findings extend the understanding of excitable systems, demonstrating how thermal and feedback mechanisms interplay to shape nonlinear optical dynamics. Further, our approach paves the way for the study of cavity stabilization and cavity cooling using an additional control beam.

I. INTRODUCTION

The phenomenon of excitability is a key concept across various research fields that has attracted considerable attention over the last decades [1–5]. A list of examples includes biological systems such as neurons in the human brain [6], chemical reactions like the Belousov-Zhabotinsky reaction [7], neuro-inspired computing [8, 9], cardiac arrhythmias [10, 11], fluid systems such as faraday waves [12, 13], lasers [14] or extreme weather events [15], to name just a few. There, excitations can be found in a purely temporal domain, however, spatially propagating excitations such as spiral waves, observed e.g., in the context of cardiac arrhythmias [10], liquid crystals [16], or two-dimensional vertical-cavity surface-emitting lasers (VCSELs) [17] can be found.

In this paper, we investigate the influence of thermal effects on the dynamics of a vertically emitting Kerr-micro-cavity operated in the Gires–Tournois regime (KGTI) [18–23] that is subjected to strong time-delayed optical feedback and detuned optical injection, see Fig. 1. To this aim, we derive a delay algebraic equations (DAEs) model including the effects of thermal expansion and temperature dependent refractive index. In particular, we report and analyze the occurrence of *excitable thermo-optical pulses* (TOPs) in a higher-dimensional canard scenario, featuring relaxation- and mixed-mode oscillations (MMOs) [24–26]. We find that temporal localized states with a period of approximately one round-trip in the external cavity, previously observed in the KGTI system without thermal effects [19, 20] still manifest themselves as stable periodic solutions, while also TOPs and relaxation oscillations can be observed, featuring oscillatory

details that evolve on the timescale of the round-trip in the external cavity.

In the framework of optical systems, excitability was studied theoretically and observed experimentally in e.g., lasers with optical feedback [17, 27–30], injected lasers [29, 31–33], lasers with saturable absorber [14, 34, 35], Fabry-Perot cavities [36, 37], semiconductor ring laser systems [38] and all-fiber lasers [39]. In particular, excitability manifests itself in studies of the so-called low-frequency fluctuations observed in the laser output. These fluctuations appear as abrupt decreases in intensity almost to zero, followed by a slow recovery [27, 28, 40]. Additionally, a canard scenario corresponding to the excitability transition in the van der Pol-FitzHugh-Nagumo model has been observed in the thermo-optical dynamics of semiconductor optical amplifiers (SOAs) and VCSELs [40–42]. Here, excitability occurs due to the major thermal effects in optical microcavities: thermal expansion [36] and temperature dependent refractive index [43]. Both effects mentioned enter the dynamics in a similar way by changing the effective cavity length, affecting the microcavity resonance and ultimately the detuning. As these effects are significantly slower than the other intrinsic timescales of the optical systems, they introduce a drastic scale separation [9] responsible for the observation of excitability. As such, this work on thermal effects provides an important first step towards the investigation of thermal cavity stabilization and cavity cooling, which can be approached using an additional control beam and a secondary resonance as discussed in more detail in [43]. In general, a dynamical system is considered to be excitable if its unique stable steady state, in this context also referred to as the quiescent state [6], may respond to an external perturbation in two different ways: If the perturbation amplitude surpasses a certain small threshold, the system responds with a macroscopic excursion through the phase

* Corresponding author: elias.koch@uni-muenster.de

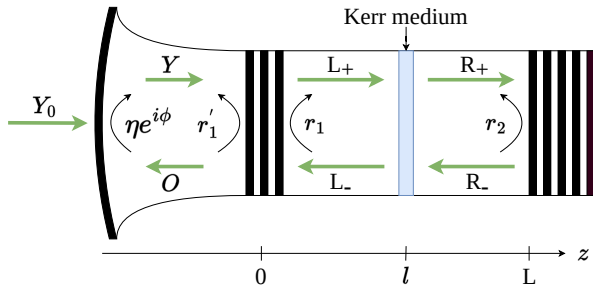


FIG. 1. Schematic of a micro-cavity containing a Kerr medium at $z = l$ closed by distributed Bragg mirrors at $z = 0$ and $z = L$. It is subjected to optical feedback from an external cavity closed by a mirror with reflectivity η and phase ϕ . The compound cavity system is driven by a continuous wave injection beam with amplitude Y_0 . The reflection coefficients are indicated by $r_{1,2}$ for the left and right mirrors, respectively, whereas the prime mark reflection and transmission processes originating from outside of the micro-cavity. The intracavity field is split into left L_{\pm} and right R_{\pm} counter-propagating waves on each side of the the Kerr slice.

space. Alternatively, it relaxes exponentially to the quiescent state in response to perturbations below the threshold. The large amplitude response, whose shape depends only weakly on the details of the initial perturbation, is followed by a refractory time, during which the system ignores further perturbations. Excitable orbits typically occur in systems with at least two well-separated timescales. The presence of excitability is usually a sign of proximity to a region of self-sustained relaxation oscillations whose shape and amplitude are related to that of the excitable orbits. The respective bifurcation scenarios, that connect the quiescent state to the relaxation oscillations, are particularly interesting, since they have to contain a sharp transition to the large-amplitude orbits. The most common scenarios are a saddle-node bifurcation on an invariant circle (SNIPER, or Andronov bifurcation) or an Andronov-Hopf (AH) bifurcation [6]. In the AH scenario, one might expect a subcritical bifurcation and, indeed, this is a scenario in the Hodgkin-Huxley model for neural excitability [6] or resonant tunneling diodes [44]. However, excitability can also occur in a supercritical AH scenario, well known from the van der Pol-FitzHugh-Nagumo model [45, 46], which is a simplified model for neuron dynamics. Here, a narrow regime of subthreshold oscillations emerges at the primary bifurcation [47], followed by an abrupt though continuous increase of amplitude and period. This phenomenon, known as a canard explosion, leads to the relaxation oscillation regime. Note that subthreshold oscillations can still exhibit excitations if perturbed above the respective threshold [48]. This comparably simple scenario drastically changes if a third variable, such as inertia, is added to the system [47] leading to new effects that disrupt the clear separation between subthreshold and relaxation oscillations.

II. MODEL SYSTEM

The schematic setup is depicted in Fig. 1. It is composed of a monomode micro-cavity of a few micrometers between two Bragg mirrors located at $z = 0$ and $z = L$. The corresponding reflection coefficients are $r_{1,2}$ for the top and the bottom mirror, respectively, whereas primes denote the case on the outside of the micro-cavity. The intracavity field is split into left ($-$) and right ($+$) moving waves to the left (L) and right (R) of thin slice of Kerr material that is situated at the field's anti-node at $z = l$. The micro-cavity is coupled with a long external cavity, (typically) a few centimeters in length, with a round-trip time τ . The external cavity is closed by a feedback mirror with reflectivity η and phase ϕ . The system is driven by continuous wave (CW) injection with amplitude Y_0 and frequency ω_0 . The light coupling efficiency in the cavity is given by the factor $h = h(r_1, r_2)$, where the choice of a perfectly reflecting bottom mirror ($r_2 = 1$) results in $h = 2$, which corresponds to the Gires-Tournois interferometer regime [18]. A Gires-Tournois interferometer is essentially an asymmetrical Fabry-Perot resonator, composed of one highly reflective mirror and one semi-transparent mirror. The latter are widely used as optical pulse-shaping elements, inducing a controllable amount and sign of group delay dispersion, which is the dominating effect outside resonance.

The optical properties of the cavity change with temperature. Beyond the direct thermal expansion of the crystal, the thermo-optical effect represents the change in refractive index with temperature [49]. Both effects lead to a change of the cavity resonant frequencies ω_c . The direction and the strength of this effect depends on the material itself. For a microcavity injected with a field of amplitude Y_0 and frequency ω_0 , the microcavity resonance is incorporated into the model through the detuning $\delta = \omega_c - \omega_0$. As we include thermal effects, ω_c becomes a time-dependent variable through the evolution of the temperature, driven by optical absorption acting as a heat source. Following the lines of [19, 37] we can derive the model equations (see App. A for details) as

$$\dot{E} = [-1 + i(s|E|^2 - \delta)]E + hY, \quad (1)$$

$$\dot{\delta} = \gamma(\delta_0 - \delta - \mu_\alpha |E|^2), \quad (2)$$

$$Y = \eta e^{i\phi} [E(t - \tau) - Y(t - \tau)] + \sqrt{1 - \eta^2} Y_0. \quad (3)$$

Here, E and Y denote the slowly varying envelopes of the electric fields in the micro-cavity and the external cavity, respectively. The cavity-enhanced nonlinear coefficient s is in general complex and its real and imaginary parts model the effects of the self-phase modulation and two-photon absorption, respectively. Further, δ_0 denotes the intrinsic detuning with respect to the microcavity resonance in the absence of the heat sources. The thermal inertia of the cavity is denoted by γ while μ_α represents the thermal nonlinearity of the cavity, with μ_α in m^2/V^2 . The latter depends on the thermal impedance,

the absorption, as well as the thermo-optic coefficients. As in [37], the net amount of absorbed light is obtained by performing an energy balance between the norm of the Poynting vectors associated with the incoming and emitted fields, see App. A for details. The field cavity enhancement can be conveniently scaled out using Stockes relations allowing the intracavity and external cavity fields, E and Y , to be of the same order of magnitude. This leads to the simple input-output relation $O = E - Y$. The coupling between the intra-cavity and the external cavity fields is given in Eq. (3) by a DAE where the effects of the external mirror and signal extraction (e.g., a beam-splitter or transmission through the mirror itself) are combined in the attenuation factor η . The total phase upon re-injection is $\varphi = \omega_0\tau + \phi$ consisting of the accumulated phase per round-trip due to propagation and the feedback mirror phase ϕ . Finally, throughout our simulations, we apply Gaussian white noise with an amplitude of σ to the fast E -field to observe excitability.

III. THERMO-OPTICAL EXCITATIONS FOR SHORT EXTERNAL CAVITY

A. Excitability through manipulating the nullclines

We note that the introduced thermal evolution given by Eq. (2) is typically much slower than the round-trip time τ in the external cavity. Hence, to isolate the impact of thermal effects on the KGTI system, we first consider the limit $\tau \rightarrow 0$. This limit corresponds to a simple injected Kerr micro-cavity, reducing the DAE system (1)-(3) to a system of ordinary differential equations (ODEs)

$$\dot{E} = \left[i(s|E|^2 - \delta) + \frac{h\eta e^{i\varphi}}{1 + \eta e^{i\varphi}} - 1 \right] E + \frac{h\sqrt{1 - \eta^2}}{1 + \eta e^{i\varphi}} Y_0, \quad (4)$$

$$\dot{\delta} = \gamma (\delta_0 - \delta - \mu_\alpha |E|^2). \quad (5)$$

The zeros of the right-hand sides of Eqs. (4),(5) define the so-called nullcline curves of the system and Fig. 2 (a) shows the E -nullcline for the intensity field $|E|^2$ of Eq. (4) as a function of the thermal detuning δ for different values of s , that we consider here to be real for simplicity. One can see that the nullcline without the Kerr effect (i.e. $s = 0$) does not possess any folds, which excludes the possibility of bistability, whereas the bending of the nullcline curve away from the symmetric case $s = 0$ equals the strength of the Kerr effect s .

Note that the full phase space $(\delta, \theta, |E|^2)$ of the system (4)-(5) is three-dimensional, where θ is the phase of the E -field. Hence, since (2) is phase-invariant, the corresponding δ -nullcline of Eq. (5) is actually a plane. Figure 2 (b) presents the E -nullcline for $s = 1$ together with the δ -nullclines for three different values of μ_α which directly determines the slope of the plane. One notices

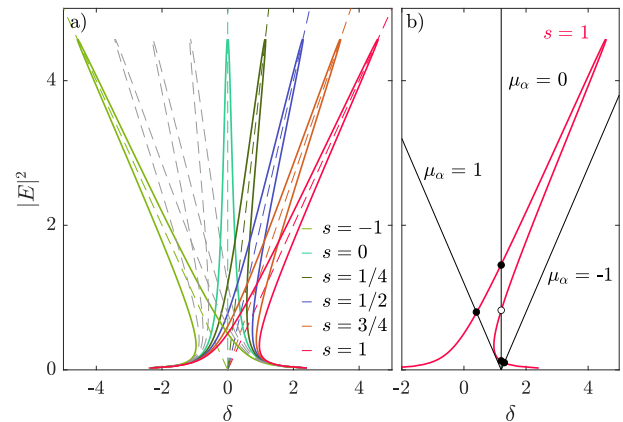


FIG. 2. a) A E -nullcline of Eqs. (4),(5) for different values of s . The nullcline is bent away from the vertical position for $s = 0$, enabling a bistable CW response in for the system. b) (E, δ) -nullclines for $s = 1$ for different values of μ_α (black). The intercepts of both curves corresponds to stable (filled circle) and unstable (open circle) fixed-points of the CW solution. Parameters are: $(\delta_0, h, \eta, \varphi, Y_0, \gamma) = (1.2, 2, 0.7, 0, 0.45, 0.01)$.

that by for example changing μ_α and keeping δ_0 fixed, the number, position, and stability of the fixed points resulting from the intercepts of the nullclines can be tuned. We start by considering a parameter set corresponding to a single stable fixed point (cf. Fig. 2 (b) for $\mu_\alpha = -1$) and fix the thermal scale $\gamma = 0.01$, thus allowing for a time-scale separation between the field and the thermally controlled detuning. We performed numerical simulations of Eqs. (4)-(5) in the presence of noise. In this regime, the system exhibits TOPs on top of the stable CW state, as presented in Fig. 3. Here, panel (a) shows the field intensity of the resulting time trace with pronounced excitations initiated by noise. Figure 3 (b) contains a zoom into a single excitation pulse. Here, the dashed black line corresponds to the δ -values and for the E -field profile one recognises the so-called fast (red) and slow (blue) stages, caused by multiple time-scale dynamics.

The origin of the slow and fast stages is illustrated in panel (c), where the pulse profile is shown in the $(\delta, |E|^2)$ projection of phase space, along with the E -nullcline (black) and the δ -nullcline (light blue). The stable fixed point marked as A is at the intercept of both curves. A sufficiently strong perturbation can push the trajectory beyond the separatrix between the basin of attraction of the fixed point A and the upper branch of the nullcline. Above the δ -nullcline, there is only dynamics towards positive δ direction (blue arrow), however, since δ is a slowly evolving variable, the trajectory is rapidly pulled towards the upper branch of the E -nullcline in a fast stage AB , preventing a return to the fixed point. As the trajectory approaches the E -nullcline, the dynamics of the field E is enslaved by the slow variable δ , initiating the slow stage BC , where $\delta \approx |E|^2$ holds. At the upper fold of the E -nullcline, point C , the trajectory can no

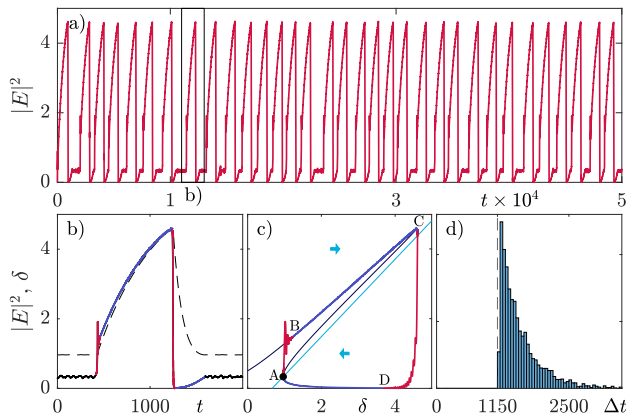


FIG. 3. Excitable thermo-optical pulses on top of the stable continuous wave state. a) A typical numerical time trace of Eqs. (4)-(5) with several excitations initiated by noise. b) Single excitation with fast (red) and slow (blue) stages for the E field, caused by multiple timescale dynamics. The δ field is depicted in dashed black. c) The same pulse in the $(\delta, |E|^2)$ projection of the phase space together with the E -nullcline (black) and the δ -nullcline (light blue). d) The corresponding interspike interval histogram. Parameters are $(\delta_0, h, \eta, \varphi, Y_0, \mu_\alpha, \gamma, s) = (0.665, 2, 0.7, 0, 0.45, -0.9, 0.01, 1)$.

longer follow the nullcline because the phase space region above the δ -nullcline is constrained to flow in the positive δ direction. Hence, the trajectory departs from the nullcline, initiating the fast stage CD , characterized by oscillatory dynamics to be discussed later. Finally, near point D , the trajectory reaches the lower branch of the E -nullcline, starting another slow stage DA that returns to the fixed point A . Panel (d) shows the corresponding interspike-interval (ISI) histogram [50]. There, one can see the characteristic cutoff at $\Delta t \approx 1150$ due to the refractory time and an exponential decay in the likelihood of longer interspike intervals. For this and all subsequent ISI histograms, the interspike intervals of a time trace featuring approximately 6000 excitations were evaluated by calculating all peak-to-peak distances and sorting them into discrete, equidistant bins. It is normalized in a way that all bars sum up to one.

A slight reduction in δ_0 can shift the fixed point A to the upper fold, see Fig. 4 (c) where the system is monostable once again. In the presence of noise, we now observe dark TOP excitations, or dropouts, as depicted in Fig. 4 (a,b), occurring on the upper CW value. These excitations have a longer refractory time, resulting in a larger cutoff in the ISI histogram, as shown in Fig. 4 (d). This is due to the δ -nullcline being closer to the slow stage DA . Additionally, the ISI histogram appears to exhibit a smoothed cutoff, likely due to the noise amplitude being below the coherence resonance. According to the concept of coherence resonance, there exists an optimal noise amplitude leading to an almost periodic train of excitations, with adjacent excitations occurring nearly immediately after recovery. In this case, the ISI histogram displays a max-

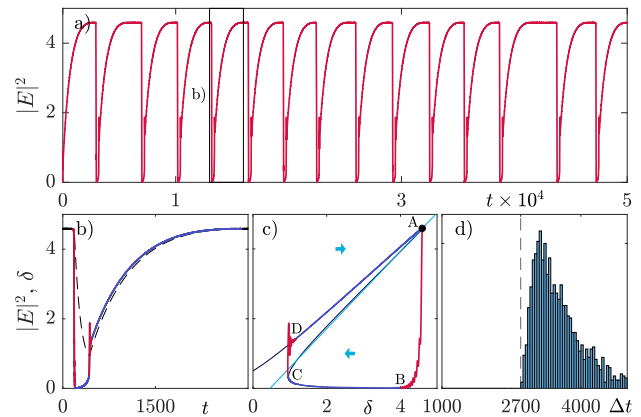


FIG. 4. Dark excitable thermo-optical pulses on top of the upper stable continuous wave state obtained by numerical integration of Eqs. (4)-(5) for $\delta = 0.46$. a) A typical numerical time trace with several excitations initiated by noise. b) Single excitation with fast (red) and slow (blue) stages, caused by multiple timescale dynamics. The δ field is depicted in dashed black. c) The same pulse in the $(\delta, |E|^2)$ projection of the phase space together with the E -nullcline (black) and the δ -nullcline (light blue). d) The corresponding interspike interval histogram. Other parameters as in Fig. 3.

imum peak near the recovery time, followed by an exponential decay. Note that the ISI histogram of a periodic solution contains only a single peak at the corresponding period.

Interestingly, the refractory time for dark excitations is significantly longer than that for bright excitations. This is primarily due to the prolonged slow stage along the upper branch of the E -nullcline, caused by the reduced distance to the left-shifted δ -nullcline in the dark TOP case, reducing the velocity of this slow stage even further. Consequently, the other slow stage is shorter in the dark case. However, since this stage is generally relatively short for dark and bright excitable TOPs alike, the total excitation period is still increased.

B. Enslaved and unbound phase dynamics

Figure 5 illustrates the full three-dimensional phase space $(\delta, \theta, |E|^2)$ of Eq. (4) (dark blue) and Eq. (5) (shaded plane). The green circle A indicates the single stable fixed point located at the intercept of the nullclines. Additionally, the trajectory of a bright TOP, as depicted in Fig. 3 (b), is represented here with red and blue segments denoting fast and slow stages of the dynamics, respectively.

The full phase dynamics along the excitation trajectory reveal rotational motion in the $(|E|^2, \theta)$ plane. This phase rotation is primarily influenced by the term $i(-\delta + |E|^2)$ from Eq. (4) for $s = 1$. During the slow stage BC , $\delta \approx |E|^2$ holds, as visible in Fig. 3 (b), causing the phase rotation to vanish, i.e. the phase is enslaved.

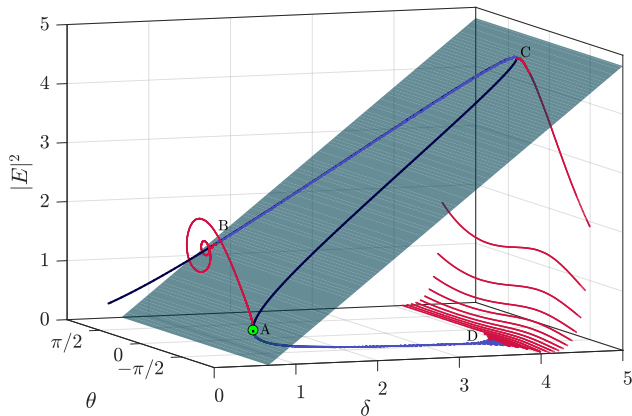


FIG. 5. The trajectory of the bright excitable TOP (cf. Fig. 3) (red for fast (AB , CD) and blue for slow (BC , DA) stages, respectively) in the three-dimensional phase space (δ , θ , $|E|^2$). The E -nullcline is given by a dark blue line, as the real and imaginary parts of E have a fixed relation on the nullcline. The δ -nullcline does not depend on the phase θ , hence it is a plane in the phase-space. The green circle at A marks the single stable fixed point located at the intercept of the nullclines. Parameters as in Fig. 3.

Upon reaching point C , where $\delta_C \approx |E_C|^2$, the intensity rapidly decreases during the adjacent fast stage. Owing to the time-scales separation governed by γ , the detuning δ remains approximately constant at a value δ_C during the relaxation of E . Consequently, the rotational velocity increases towards $i(-\delta_C)$, causing the rise in oscillation speed in negative θ -direction observed in the fast stage CD in Fig. 5.

The fast stage ends as the trajectory approaches the lower branch of the E -nullcline, initiating a second slow recovery stage DA that returns to the fixed point. Since the maximum rotation is proportional to δ_0 , the oscillations occurring along the fast stage can be tuned by selecting a parameter regime with smaller δ_0 . As δ_0 represents the detuning between the micro-cavity resonance without thermal heating ω_c and the injection frequency ω_0 , it can be modified by tuning the external injection frequency.

C. Accessing different dynamical regimes

As already discussed above, the form of the E -nullcline is influenced by the parameters η , φ , Y_0 as well as the strength of the Kerr effect s . However, the way these parameters enter the nullcline is not trivial. This is different for the δ -nullcline following the simple equation $\delta = \delta_0 - \mu_\alpha |E|^2$. One can observe that δ_0 is the δ -intercept while μ_α represents the slope. By tuning the injection frequency, i.e. δ_0 , we are able to shift the δ -nullcline and change the behavior of the system in question. An overview over four different dynamical regimes that can be accessed by tuning a single parameter is shown in

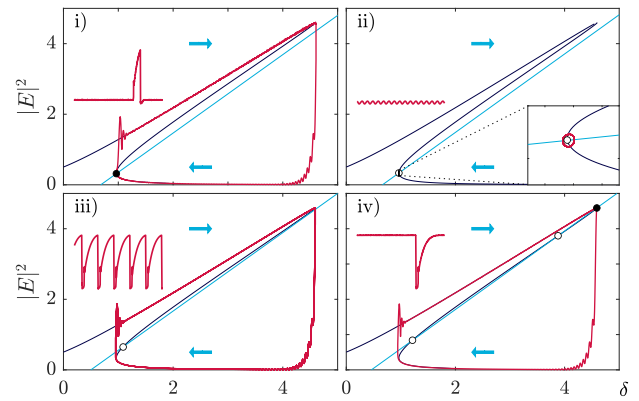


FIG. 6. Different dynamical regimes obtained numerically from Eqs. (4, 5) (red line) in the (δ , $|E|^2$) phase space for four different values of δ_0 : (i) bright TOP; (ii) subthreshold oscillations; (iii) relaxation oscillations; (iv) dark TOP. The E - and δ nullclines are depicted in dark and light blue, respectively. Black filled (open) circle mark stable (unstable) fixed point. σ indicates the amplitude of the Gaussian white noise. Other parameters as in Fig. 3.

Fig. 6. Here, each panel depicts the (δ , $|E|^2$) projection of the phase space together with the E -nullcline (dark blue) and the δ -nullcline (light blue). The blue arrows indicate the flow direction induced by the δ -nullcline. Note that it can be drawn into the two-dimensional projection, since the corresponding nullcline is invariant with respect to the phase. For the E -nullcline this is different, since the flow strongly depends on the explicit value of the phase, for example leading to oscillation around the one-dimensional E -nullcline. However, the flow direction induced by the δ -nullcline together with the position and number of stable (black filled circle) and unstable (black open circle) fixed points already allows to predict the systems behavior. In particular, Fig. 6 (i) shows the scenario of a single stable fixed point close to the lower fold of the E -nullcline. As discussed in Fig. 3, time simulation devoid any noise or other perturbations will end and stay on this fixed point. However, bright excitable TOPs (red curve) are possible by adding noise to the E -field of Eq. (4). If δ_0 is slightly decreased, the fixed point is losing its stability and subthreshold oscillations can arise in a canard scenario close to the primary supercritical AH bifurcation, see Fig. 6 (ii). Further, it is possible to excite the system on top of the subthreshold oscillation, if it is perturbed above the threshold and if δ_0 is further reduced, a sharp transition of period and amplitude is observed, leading to a regime of self-sustained relaxation oscillations, which are shown in panel (iii). At some point, for even smaller values of δ_0 , a pair of stable and unstable fixed-points appears around the top fold of the E -nullcline as shown in panel (iv). Here, dark excitable TOP set in if noise is applied, cf. Fig. 4. The further the stable fixed point departs from the fold, the stronger perturbations are necessary to produce these excitations.

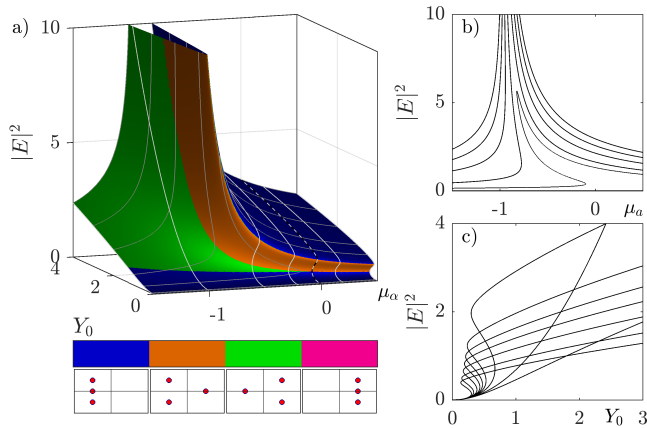


FIG. 7. (a) CW solution of Eqs. (4,5) in the (μ_α, Y_0) plane. The colors encode the stability information as indicated in the legend at the bottom: blue, orange, green and magenta correspond to stable, saddle-node unstable, AH unstable as well as fully unstable CW, respectively. The grey lines are cuts in the one-parameter planes $(\mu_\alpha, |E|^2)$ and $(Y_0, |E|^2)$ and are shown in panels (b) and (c), respectively. Parameters are $(\delta_0, h, \eta, \varphi, \gamma, s) = (1, 2, 0.7, 0, 0.01, 1)$.

For an even smaller value of δ_0 , the stable fixed point is no longer in the bistable regime and vertical perturbations through noise applied to Eq. (4) cannot produce any hysteresis behavior anymore.

D. Bifurcation analysis

To further investigate the stability regions of excitable TOPs and how they emerge, we perform a bifurcation analysis of the dynamical scenarios observed in Fig. 6. First, setting $(\dot{E}, \dot{\delta}) = 0$ in the system (4,5), one can analytically calculate the emerging CW solutions and determine their linear stability, see Fig. 7. In panel (a) the intensity of the CW solution is plotted over the (μ_α, Y_0) plane, whereas the corresponding cuts in μ_α and Y_0 -directions are shown in panels (b) and (c), respectively. The colors in Fig. 7 (a) represent the different types of instabilities, characterized by three discrete eigenvalues, see the bottom panel. In particular, a stable steady state (blue) can lose its stability in either a saddle-node bifurcation leading to a single real eigenvalue crossing the imaginary axis (orange) or a AH bifurcation (green), where a real part of the pair of complex eigenvalues changes its sign. Alternatively, all three eigenvalues can become unstable (magenta), however, this scenario is not realized for the parameters presented in Fig. 7.

We note that the AH unstable region can host both stable large amplitude relaxation oscillations and the narrow subthreshold oscillation regimes (cf. Fig. 7 (ii,iii)), whereas excitability regimes shown in Fig. 7 (i,iv) can be expected to occur close to the AH bifurcation line for negative values of μ_α . Indeed, in the focusing regime, where

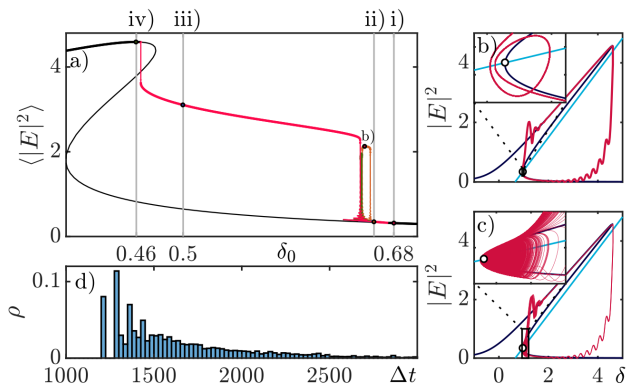


FIG. 8. Bifurcation diagram obtained for $\gamma = 0.05$ as a function of δ_0 . The branch of relaxation oscillations (red) emerges from the stable CW branch (solid black) in a supercritical AH bifurcation. Here, the subthreshold oscillation regime is very small, followed by a sharp Canard transition. After an extended relaxation-oscillation regime, another transition is entered, with a complex mixed-mode oscillation scenario. Grey vertical lines (i-iv) correspond to the dynamical regimes in Fig. 6. b) Mixed mode oscillations with one subthreshold period. c) Deterministic random spiking due to a non-periodic attractor on the subthreshold branch surpassing the excitability threshold. Other parameters as in Fig. 3.

the strength of the Kerr effect s is positive, hysteresis behavior can only be found if the δ -nullline is tilted into the same direction, which is the case for $\mu_\alpha < 0$, cf. Fig. 2. In its turn, for negative s , one would get excitability for $\mu_\alpha > 0$. Further, one can see that for a large negative $\mu_\alpha < 0$, the AH unstable regime seems to extend over an increasing Y_0 range, cf. Fig. 7. Since the bistability is lost at $\mu_\alpha = -1$, there are no dark excitable TOPs or dropouts to be expected beyond $\mu_\alpha = -1$. In the next step, we fix μ_α and perform numerical path continuation. However, the small phase oscillations caused by the unbound phase dynamics in the fast stage of relaxation oscillations demand profiles with a highly refined mesh. Furthermore, continuation software often struggles to converge for extremely detailed solutions. For this reason, we reduce the scale separation, effectively decreasing the duration of relaxation oscillations by setting $\gamma = 0.05$. Resulting branches are depicted in Fig. 8 as a function of δ_0 . Here, vertical grey lines indicate corresponding dynamical regimes shown in panels (i)-(iv) in Fig. 6. One can see that for large values of δ_0 , the CW solution is stable (black thick line). However, decreasing δ_0 , a branch of periodic solutions (red) emerges close to point i) (bright excitable TOPs) in a supercritical AH bifurcation. Here, subthreshold oscillations (cf. point ii)) with a small period and amplitude emerge. Note, that applying noise on these periodic solutions will still produce bright excitable TOPs. Reducing δ_0 further results in a canard explosion towards high oscillation amplitudes and periods leading to the formation of relaxation oscillations as at point iii). Further, another canard explosion at smaller values of δ_0 results in a small region of subthreshold pe-

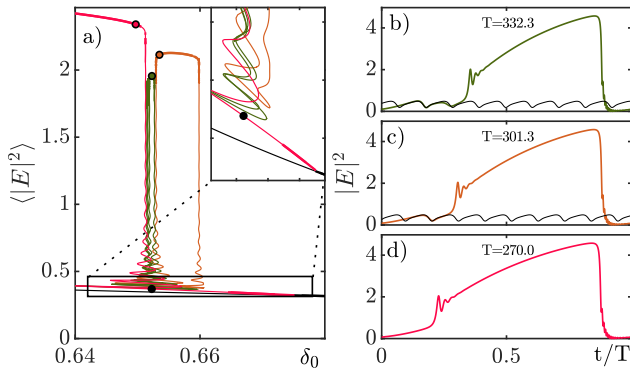


FIG. 9. Zoom around the Canard explosion region found for $\gamma = 0.05$ as a function of δ_0 . As the subthreshold oscillations (red) experience a period doubling bifurcation, they lose stability, while different mixed-mode oscillation branches (green, orange) emerge. (b-c) show exemplary profiles of mixed-mode oscillations at positions marked by filled circles featuring $n = 2, 1$ periods of the subthreshold oscillation. d) exemplary profile of the relaxation oscillation. Other parameters as in Fig. 3.

riodic oscillations around the upper CW branch, that finally becomes stable again in another supercritical AH bifurcation. Close to this point, dark excitable TOP can be formed in the presence of noise, see iv). Remarkably, as we approach the point along the vertical part of the periodic branch, where it passes the middle CW level, the period diverges, hinting an incomplete homoclinic as reported in [51] (cf. App. B for more details).

Figure 9 (a) shows a zoom into the bifurcation diagram presented Fig. 8 around the canard explosion region at large δ_0 . In this region, the branch of threshold oscillations (red) loses its stability in a period doubling bifurcation (cf. a blue branch in the inset of Fig. 9 (a)) and experiences a number of saddle-nodes bifurcations, finally resulting in a canard explosion. Here, additional two branches (green and orange) are shown that also feature stable oscillations with high amplitude and period. These solutions correspond to MMOs [24–26], featuring an integer number of subthreshold oscillations followed by a large spike.

This behavior can be understood by looking at Fig. 9 (b-d), where field intensity profiles over one period from each branch at the positions marked by filled circles (colored accordingly) are depicted. The black thin lines in panels (b-c) indicate the subthreshold oscillation solutions, taken from the δ_0 value marked with a filled black circle that is visible in the insert in Fig. 9 (a). Figure 9 (d) shows the relaxation oscillations at the unstable CW solution. In contrary, in panel (c), a single period of the subthreshold oscillations appears additionally (cf. also Fig. 8 (b) for the phase space dynamics), while in panel (b) two additional periods of the subthreshold oscillation are observed. The period T increases by 30 with each added subthreshold period which corresponds ap-

proximately to the period of the latter.

Note that all shown profiles in Fig. 9 (b-d) belong to stable parts of their respective branches and are thus accessible for numerical time simulations. This is shown in Fig. 8 (b), depicting a numerical solution for a δ_0 value from the orange branch in Fig. 9 (c), indeed leading to the respective MMOs (cf. the inset of Fig. 8 (b)). In general MMOs can occur, when the subthreshold oscillations, for instance as result of a period-doubling bifurcation, surpass the threshold after an integer, in the case of chaotic spiking random, number of oscillation periods [25]. In the present scenario, a cascade of period-doubling bifurcations, each introducing higher order MMOs, can result in a chaotic attractor on the subthreshold branch, surpassing the threshold in a non-periodic sequence. This allows for the observation of chaotic spiking in the absence of any noise as depicted in Fig. 8 (c). The respective ISI histogram in Fig. 8 (d) indicates the characteristic complex structure with multiple peaks resulting from the oscillatory structure of the chaotic attractor as in [47].

IV. IMPACT OF THE EXTERNAL CAVITY

Our analysis demonstrated that a more realistic modeling including thermal effects leads to a wealth of new regimes. It is therefore justified to wonder if all the localized state solutions and their associated frequency combs can still be observed in this system. In particular, in the presence of the external cavity and in the absence of thermal effects (i.e. for $\mu_\alpha = 0$), multistable bright and dark temporal localized states (TLSs) can be formed in the KGTI system (1-3) in the normal dispersion regime via the locking of domain walls connecting the high and low intensity levels of the injected micro-cavity [19, 20]. Note that as even if the external cavity can be as long as several centimeters, the thermal timescale remains much longer than the cavity round-trip. Hence, in the following we focus on the regime where $\gamma^{-1} \gg \tau > 1$, setting time-delayed feedback on a time scale between the slow thermal effects and the fast micro-cavity dynamics. Further, we are interested in the impact of the external cavity on the formation of excitable TOPs. We fix μ_α to a value yielding one stable fixed point (cf. Fig. 2 (b) for $\mu_\alpha = -1$) and perform numerical simulations of Eqs. (1-3) in the normal dispersion regime. Our results are presented in Fig. 10 (a), where the τ -periodic train of bright TLS is shown in red, while the blue dashed line corresponds to the time evolution of the thermal detuning δ . Remarkably, in this regime, the thermal effects allow TLSs to remain stable outside of the bistability region since for $\mu_\alpha = -1$ the bistability is lost (cf. Fig. 2 (b)). The absence of the bistability changes the nature of the resulting TLS as they were previously born from locking of fronts between two stable CW values, whereas now they are homoclinic orbits living on a monostable CW background (cf. the inset in Fig. 10 (a)). Consequently, the dark TLSs observed for the same parameter

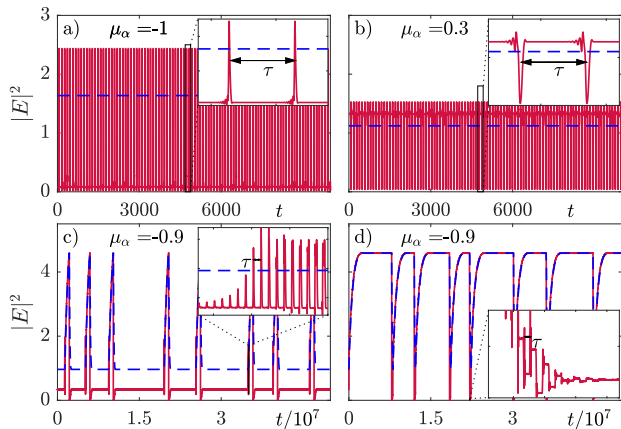


FIG. 10. Time simulations of Eqs. (1-3) for $\tau = 100$. (a,b) Stable bright and dark TLSs for $\gamma = 10^{-4}$ and $(\delta_0, h, \eta, \varphi, Y_0) = (1.5, 2, 0.75, 0, 0.6/0.38)$. (c,d) Thermo-optical excitability observed for $\gamma = 10^{-5}$ and other parameters as in Fig. 3 (Fig. 4).

set [20] cannot be stabilized for $\mu_\alpha = -1$ as they live on the, now non-existing, upper CW background. However, they can be found for smaller values of μ_α as shown in Fig. 10 (b) for $\mu_\alpha = 0.3$.

Finally, bright and dark TOP excitations can be observed for the same parameter set as in Fig. 6 in the presence of the external cavity, see Fig. 10 (c,d), respectively. Here, a new phenomenon can be observed, as the small oscillations caused by the phase dynamics are now oscillating with a period close to the delay time τ . In particular, in the inset of Fig. 10 (c), these oscillations even resemble TLSs that might occur temporarily due to the slow δ dynamics as they pass certain parameter values. The occurrence of both timescales in the same orbit clearly indicates how these timescales are able to interact.

However, the excitability seems to vanish if δ does not evolve on the slowest timescales. This observation is supported if γ is increased to e.g., $\gamma = 10^{-4}$, leading to a situation where the excitability competes with a τ periodic solution (cf. Fig. 10 (a,b)). Considering another limit case, where $\tau \gg \gamma^{-1}$, excitable orbits would turn into periodic solutions, as the excitation would travel through the external cavity while the thermal dynamics would fully relax. As a result, the optical feedback would excite the system repeatedly after each round-trip. However, this scenario is of no experimental use for this specific setup.

V. CONCLUSION

We investigated the influence of thermal effects on the dynamics of a vertically emitting micro-cavity with a Kerr nonlinearity, subjected to detuned optical injection and coupled to a long external cavity. As the microcav-

ity heats in the presence of light, the reflective index and with that the micro-cavity resonance evolve on a slow time scale. Consequently, the detuning between injection frequency and micro-cavity resonance turns into a dynamical variable. To isolate the influence of thermal effects, we started with a vanishing delay case, reducing the system to a three-dimensional ordinary differential equation. Here, we find excitability close to a supercritical canard scenario. In the vicinity of a bistable continuous wave (CW) regime caused by the Kerr nonlinearity, we observed dark and bright excitability on the higher and lower CW background, respectively. In the bright case, mixed-mode oscillations and even chaotic spiking were demonstrated. Finally, we added an external cavity with a delay that is long compared to the neglected microcavity delay, but short compared to the thermal timescale. We confirmed, that localized states observed in previous works continue to exist, if thermal effects are included, while the new relaxation oscillation regimes create stable localized states beyond the CW bistability. This shall act as an outlook on future investigations regarding the interaction between delay and thermal effects. Finally, our extended model is a first step towards elaborating strategies regarding thermal cavity stabilization and cavity cooling using, e.g., an additional control beam and a secondary resonance as detailed in [43].

ACKNOWLEDGMENTS

Funding J.J. acknowledges the financial support of the project KEFIR/AEI/10.13039/501100011033/ FEDER, UE. E.R.K, J.J. and S.V.G. acknowledge the financial support of the project KOGIT, Agence Nationale de la Recherche (ANR-22-CE92-0009), Deutsche Forschungsgemeinschaft (DFG) via Grant Nr. 505936983.

Disclosures The authors declare no conflicts of interest

Data availability Data underlying the results presented in this paper are not publicly available at this time but may be obtained from the authors upon reasonable request.

Appendix A: Model derivation

We derive in this section the Kerr Gires-Tournois interferometer model from first principles giving particular attention to how thermal effects are included. We start from the Maxwell equations for the real electric and magnetic fields so that $(\mathcal{E}, \mathcal{B}) \in \mathbb{R}^3$. We assume a nonmagnetic material as well as the absence of free charges and free currents, yielding

$$\nabla \cdot \mathcal{D} = 0, \quad (\text{A1})$$

$$\nabla \cdot \mathcal{B} = 0, \quad (\text{A2})$$

$$-\nabla \times \mathcal{E} = \dot{\mathcal{B}}, \quad (\text{A3})$$

$$\nabla \times \mathcal{H} = \dot{\mathcal{D}}. \quad (\text{A4})$$

The auxiliary fields $(\mathcal{D}, \mathcal{H})$ are defined as

$$\mathcal{D} = \epsilon_0 \mathcal{E} + \mathcal{P} \quad (\text{A5})$$

$$\mathcal{H} = \mathcal{B}/\mu_0, \quad (\text{A6})$$

where $\mathcal{P} = \mathcal{P}_1 + \mathcal{P}_{\text{nl}}$ is the polarization, containing both the linear response of the cavity, in particular the refractive index dependence on the temperature, as well as the Kerr nonlinearity. For an isotropic and homogeneous medium, the constitutive relation for the refractive index is given by a convolution $\mathcal{P}_1 = \epsilon_0 \chi_l \star \mathcal{E}$, i.e.

$$\mathcal{P}_1(\mathbf{r}, t) = \frac{\epsilon_0}{2\pi} \int_{\mathbb{R}} \chi_l(s) \mathcal{E}(\mathbf{r}, t-s) ds \quad (\text{A7})$$

where $\chi_l(s)$ is a causal function. Assuming that the nonlinear effects are small, i.e. $\mathcal{P}_{\text{nl}} \ll \mathcal{P}_1$ we have that $\nabla \cdot \mathcal{P} \simeq \nabla \cdot \mathcal{P}_1$. Taking the divergence of Eq. A5, using Eq. A1 and noting that Eq. A7 is an integral in the time domain, we deduce that both \mathcal{E} and \mathcal{P}_1 are divergence-free, i.e. $\nabla \cdot \mathcal{E} \simeq 0$ and $\nabla \cdot \mathcal{P}_1 \simeq 0$.

In order to describe the propagation of electromagnetic waves we applying the curl operator to Maxwell-Faraday equation given in Eq. A3. Using Maxwell-Ampere equation given by Eq. A4, the result simplifies into

$$-\mu_0 \ddot{\mathcal{D}} = \nabla \times (\nabla \times \mathcal{E}). \quad (\text{A8})$$

Using the vector identity $\nabla \times (\nabla \times \mathcal{E}) = \nabla(\nabla \cdot \mathcal{E}) - \nabla^2 \mathcal{E}$ and that \mathcal{E} is approximately divergence-free we get

$$\nabla^2 \mathcal{E} - \epsilon_0 \mu_0 \partial_t^2 \mathcal{E} = \mu_0 \partial_t^2 (\mathcal{P}_1 + \mathcal{P}_{\text{nl}}). \quad (\text{A9})$$

In the rest of the work, we shall consider a quasi-monochromatic field around the carrier angular frequency of the optical injection ω_0 . We further assume that all the fields are transversely polarized, say in the y -direction, so that $\mathcal{E}(\mathbf{r}, t) = \mathcal{E}(\mathbf{r}, t) \mathbf{y}$ with \mathcal{E} a real scalar amplitude. We define the complex field envelope $E(\mathbf{r}, t)$ that is slowly evolving in time such that

$$\mathcal{E}(\mathbf{r}, t) = \frac{1}{2} [E(\mathbf{r}, t) e^{-i\omega_0 t} + \text{c.c.}] \quad (\text{A10})$$

Similarly, the linear and nonlinear polarizations can be expressed as $\mathcal{P}_{1,\text{nl}}(\mathbf{r}, t) = \mathcal{P}_{1,\text{nl}}(\mathbf{r}, t) \mathbf{y}$ with

$$\mathcal{P}_1(\mathbf{r}, t) = \frac{1}{2} [P_1(\mathbf{r}, t) e^{-i\omega_0 t} + \text{c.c.}] \quad (\text{A11})$$

where the expression of P_1 reads after using Eq. A7

$$P_1(\mathbf{r}, t) = \frac{1}{2\pi} \int_{\mathbb{R}} \epsilon_0 \chi_l(s) E(\mathbf{r}, t-s) e^{i\omega_0 s} ds. \quad (\text{A12})$$

We define the Kerr nonlinearity as $\mathcal{P}_{\text{nl}} = \epsilon_0 \chi_3(\mathbf{r}) \mathcal{E}^3 \mathbf{y}$ and we assume the Kerr medium to be located over a finite region within the cavity, which is achieved by considering that χ_3 is a function of \mathbf{r} . We define similarly

$$\mathcal{P}_{\text{nl}}(\mathbf{r}, t) = \frac{1}{2} [P_{\text{nl}}(\mathbf{r}, t) e^{-i\omega_0 t} + \text{c.c.}] + \text{h.o.t.} \quad (\text{A13})$$

where h.o.t. denotes non-resonant terms at frequencies $\pm 3\omega_0$ while the resonant contribution P_{nl} reads

$$P_{\text{nl}}(\mathbf{r}, t) = \frac{3}{4} \epsilon_0 \chi_3(\mathbf{r}) |E|^2 E(\mathbf{r}, t) \quad (\text{A14})$$

The Fourier transform operator \mathcal{F}_t is defined as

$$\mathcal{F}_t[\mathcal{A}] = \frac{1}{2\pi} \int_{\mathbb{R}} \mathcal{A}(\mathbf{r}, t) e^{i\omega t} dt, \quad (\text{A15})$$

while the inverse transform \mathcal{F}_t^{-1} reads

$$\mathcal{F}_t^{-1}[\mathcal{A}] = \int_{\mathbb{R}} \mathcal{A}(\mathbf{r}, \omega) e^{-i\omega t} d\omega. \quad (\text{A16})$$

For the sake of simplicity, we use identical letters for the function in the time and in the frequency domain. Finally, the Fourier transform of \mathcal{E} can be expressed as a function of E since

$$\mathcal{E}(\mathbf{r}, \omega) = \frac{1}{2} [E(\mathbf{r}, \omega - \omega_0) + E^*(\mathbf{r}, -\omega - \omega_0)] \quad (\text{A17})$$

1. micro-cavity with a thin nonlinear region

As light propagates along the cavity axis z we denote by $\mathbf{r}_\perp = (x, y)$ the transverse coordinates so that $E(\mathbf{r}, t) = E(\mathbf{r}_\perp, z, t)$ while $\Delta = \partial_z^2 + \Delta_\perp^2$. Considering only the positive frequencies in Eq. A9 we find in the temporal Fourier domain that

$$\left(\partial_z^2 + \Delta_\perp^2 + \frac{\omega^2}{v^2} \right) E(\mathbf{r}_\perp, z, \omega - \omega_0) = -\mu_0 \omega^2 P_{\text{nl}} \quad (\text{A18})$$

where we defined the frequency dependent velocity $v^2 = [c/n(\omega)]^2$ and the frequency dependent refractive index $n(\omega) = \sqrt{1 + \chi(\omega)}$. We consider a thin Kerr slice of width W located in $z = l$ that we model as $\chi_3(\mathbf{r}) = \bar{\chi}_3 W \delta(z - l)$. Taking the transverse Fourier transform of Eq. A18 so that $\Delta_\perp^2 \rightarrow -q_\perp^2$ and integrating around $z = l$ over a range 2ϵ leads to

$$\partial_z E(\mathbf{q}_\perp, z, \omega - \omega_0) \Big|_{l-\epsilon}^{l+\epsilon} + \int_{l-\epsilon}^{l+\epsilon} \left(\frac{\omega^2}{v^2} - q_\perp^2 \right) E(\mathbf{q}_\perp, z', \omega - \omega_0) dz' = -\frac{3\omega^2 \bar{\chi}_3 W}{4c^2} \mathcal{F}_{t,\perp} [|E|^2 E(\mathbf{r}_\perp, l, \omega - \omega_0)] \quad (\text{A19})$$

The next step of our derivation consists in splitting the electromagnetic field in each part of the cavity before and after the Kerr slice. For a micro-cavity of length L with a nonlinear medium placed at $z = l$ we define

$$E(\mathbf{q}_\perp, z, \omega) = \begin{cases} L(\mathbf{q}_\perp, z, \omega) & 0 < z < l \\ R(\mathbf{q}_\perp, z, \omega) & l < z < L, \end{cases} \quad (\text{A20})$$

The field in each sub-section is decomposed into counter-propagating modes along the cavity axis

$$\begin{aligned} L(\mathbf{q}_\perp, z, \omega) &= L_+(\mathbf{q}_\perp, \omega) e^{iqz} + L_-(\mathbf{q}_\perp, \omega) e^{-iqz} \\ R(\mathbf{q}_\perp, z, \omega) &= R_+(\mathbf{q}_\perp, \omega) e^{iqz} + R_-(\mathbf{q}_\perp, \omega) e^{-iqz} \end{aligned} \quad (\text{A21})$$

We defined in Eqs. (A21,A22) the frequency-dependent longitudinal wave vector

$$q(\mathbf{q}_\perp, \omega) = \sqrt{\omega^2/v^2 - q_\perp^2} \quad (\text{A23})$$

The continuity of the transverse field at the boundary in $z = l$ imposes that

$$L(\mathbf{q}_\perp, l, \omega) = R(\mathbf{q}_\perp, l, \omega) = \mathbf{E}(\mathbf{q}_\perp, \omega) \quad (\text{A24})$$

where we defined $\mathbf{E}(\mathbf{q}_\perp, \omega)$ as the field amplitude impinging on the Kerr slice in $z = l$. The respective boundary condition for the derivative discontinuity imposed by the nonlinear medium taking the limit $\varepsilon \rightarrow 0$ in Eq. A19 reads

$$\partial_z R - \partial_z L = -\frac{3\omega^2 \bar{\chi}_3 W}{4c^2} \mathcal{F}_{t,\perp} \left[|\mathbf{E}|^2 \mathbf{E} \right] \quad (\text{A25})$$

where we omitted the dependence of all the variables on $(\mathbf{q}_\perp, l, \omega - \omega_0)$ for clarity.

The additional boundary conditions linking the micro-cavity with the exterior can be deduced from the setup depicted in Fig. 1. We evaluate the fields at the two extreme sides of the micro-cavity ($z = 0, L$) for which the two distributed Bragg mirrors have reflectivities in the frequency domain $r_{1,2}(\omega)$ and $t_{1,2}(\omega)$. The primed indexes are for transmission and reflection processes that originate from outside of the cavity. We assume that the DBRs have a wide bandwidth and, as such, that the modulus of the reflection coefficients do not depends on the frequency, i.e. $r_{1,2}(\omega) = |r_{1,2}| \exp[i\phi_j(\omega)]$. The output of the micro-cavity is a superposition of the reflection of the injected field as well as the micro-cavity transmission of its internal field and reads

$$O = t_1 L_- + r'_1 Y \quad (\text{A26})$$

while the intra-cavity counter-propagating waves are linked by the mirror reflectivities

$$L_+ = r_1 L_- + t'_1 Y \quad , \quad R_- e^{-iqL} = r_2 R_+ e^{iqL} \quad (\text{A27})$$

Combining Eqs. (A25,A27) allows to express (L_\pm, R_\pm) as functions of the field on the Kerr medium $\mathbf{E}(\mathbf{q}_\perp, \omega)$ and

the injected field

$$R_+ = \frac{e^{-iqL} \mathbf{E}}{1 + r_2 e^{2iq(L-l)}} \quad , \quad R_- = \frac{r_2 e^{iqL} \mathbf{E}}{r_2 + e^{2iq(L-l)}} \quad (\text{A28})$$

$$L_+ = \frac{r_1 e^{iqL} \mathbf{E} + t'_1 Y}{1 + r_1 e^{2iqL}} \quad , \quad L_- = \frac{e^{-iqL} \mathbf{E} - t'_1 Y}{r_1 + e^{-2iqL}}. \quad (\text{A29})$$

These expressions can now be inserted into the derivative boundary condition Eq. A25 which yields

$$(R_+ - L_+) e^{iqL} - (R_- - L_-) e^{-iqL} = -\frac{3\omega^2 \bar{\chi}_3 W}{4iqc^2} \mathcal{F}_{t,\perp} \left[|\mathbf{E}|^2 \mathbf{E} \right] \quad (\text{A30})$$

Upon simplification using Eqs. (A28,A29) as well as the Stokes relations ($r = -r'$, $tt' - rr' = 1$) we deduce in the transverse and temporal Fourier domains the fundamental equation linking the value of the intra-cavity field on the Kerr slice \mathbf{E} with that of the injected field impinging upon the micro-cavity Y

$$F_1 \mathbf{E} = -\frac{3\omega^2 \bar{\chi}_3 W}{8iqc^2} \Gamma \mathcal{F}_{t,\perp} \left[|\mathbf{E}|^2 \mathbf{E} \right] + F_2 Y. \quad (\text{A31})$$

where we introduced the confinement factor Γ as well as the functions $F_{1,2}$ that are characteristic of the Fabry-Perot resonator

$$\Gamma(q, \omega) = (1 + r_1 e^{2iqL}) (1 + r_2 e^{2iq(L-l)}) \quad (\text{A32})$$

$$F_1(q, \omega) = 1 - r_1 r_2 e^{2iqL}, \quad (\text{A33})$$

$$F_2(q, \omega) = t'_1 e^{iqL} (1 + r_2 e^{2iq(L-l)}). \quad (\text{A34})$$

The modes of the micro-cavity correspond to the minima of $|F_1(q, \omega)|$. They define the cavity resonances for which the intra-cavity field is maximum. This condition is achieved when

$$2q_m L = 2\pi m - [\phi_1(\omega_m) + \phi_2(\omega_m)] \quad (\text{A35})$$

where $m \in \mathbb{N}$. On another hand, the Kerr slice is placed in order to maximize the confinement factor under normal incidence, i.e. at a field anti-node. This is achieved by imposing that

$$2q_{n_1, n_2} l + \phi_1(\omega_{n_1, n_2}) = 2\pi n_1 \quad (\text{A36})$$

$$2q_{n_1, n_2} (L - l) + \phi_2(\omega_{n_1, n_2}) = 2\pi n_2 \quad (\text{A37})$$

where $n_{1,2} \in \mathbb{N}$. Notice that summing Eqs. (A36,A37) leads again to Eqs. A35 with $m = n_1 + n_2$. As such, solving Eqs. (A36,A37) allows finding all of the micro-cavity modes. The most sensible choice corresponds to placing the Kerr medium at the center of the cavity, i.e. $l = \frac{L}{2}$. In this situation, we find that one every other modes of the cavity maximizes Γ . We select the cavity mode $q_m = 2\pi m/L$ with $m \in \mathbb{N}$ for which the associated frequency ω_m , as defined by the dispersion relation $q_m = \omega_m/v(\omega_m)$, is the closest to the injection frequency ω_0 and we expand F_1 , F_2 and Γ around the mode

(q_m, ω_m) . In the good cavity limit for which $|r_{1,2}| \rightarrow 1$, the resonances are sharp and $\Gamma \rightarrow 4$ and $|F_2| \rightarrow 2t'_1$ vary much more slowly than F_1 . Noticing further that $q_m \sim L^{-1}$, we find the following hierarchy regarding the relative variation of $F_{1,2}$ and Γ

$$L^{-1}F_1^{-1}\frac{dF_1}{dq}(q_m) \sim \frac{1}{1-|r_1r_2|} \gg 1 \quad (\text{A38})$$

$$L^{-1}F_2^{-1}\frac{dF_2}{dq}(q_m) \sim 1, \quad (\text{A39})$$

$$L^{-1}\left(\frac{\Gamma}{q}\right)^{-1}\frac{d}{dq}\left(\frac{\Gamma}{q}\right)(q_m) \sim 1. \quad (\text{A40})$$

It is therefore sensible to consider only the lowest order for F_2 and Γ . However, in order to back-transform Eq. A35 to the spatiotemporal domain F_1 needs to be expanded to first order in (ω, q_\perp) . We consider small frequency variations and we assume ω to be close to a cavity mode. As the temperature varies, the refractive index $n(\omega, T)$ changes, effectively shifting the cavity length and hence the resonance frequency positions. We note that in many semiconductors such as InP, SiC or GaAs, the thermo-optic effect $\partial_T n$ is often an order of magnitude larger than the effect of thermal expansion

$L^{-1}\partial_T L$. For example in GaAs $L^{-1}\partial_T L \sim 6 \times 10^{-6} \text{K}^{-1}$ while $\partial_T n \sim 2.35 \times 10^{-4} \text{K}^{-1}$ [49]. For these reasons, we shall neglect in what follows cavity length variations due to thermal effects and we consider solely the thermo-optic effect. We allow for small temperature deviations around the equilibrium temperature T_0 and we define $\delta T = T - T_0 \ll 1$. We define $\bar{\omega}_m$ as the mode frequency when the cavity is at temperature T_0 and introduce the small deviation $\delta\omega = \omega - \bar{\omega}_m \ll 1$. The reference refractive index is $\bar{n}_m = n(\bar{\omega}_m, T_0)$ and we set $\bar{v}_m = c/\bar{n}_m$ while $\bar{q}_m = \bar{\omega}_m/\bar{v}_m$ solves Eq. A35. Finally, we allow for shallow transverse dynamics and assume that $q_\perp \ll 1$. To first order in the deviations Eq. A23 reads

$$q \simeq \bar{q}_m + \frac{\delta\omega}{v_e} + \bar{q}_m \frac{\partial_T \bar{n}_m}{\bar{n}_m} \delta T - \frac{q_\perp^2}{2\bar{q}_m}, \quad (\text{A41})$$

where we defined the effective group index velocity v_e taking into account the dispersion of the refractive index

$$\frac{1}{v_e} = \frac{1}{\bar{v}_m} + \bar{q}_m \frac{\partial_\omega \bar{n}_m}{\bar{n}_m}. \quad (\text{A42})$$

Inserting Eq. A41 in Eq. A31 and denoting $\Delta n = \partial_T \bar{n}_m \delta T$ yields

$$\mathbf{E} \left[F_1(\bar{q}_m, \bar{\omega}_m) + \partial_q F_1(\bar{q}_m, \bar{\omega}_m) \left(\bar{q}_m \frac{\Delta n}{\bar{n}_m} - \frac{q_\perp^2}{2\bar{q}_m} \right) - i\delta\omega\tau_e |r_1r_2| \right] = -\frac{3\bar{\omega}_m \bar{\chi}_3 W}{8i\bar{n}_m c} \Gamma(\bar{q}_m, \bar{\omega}_m) \mathcal{F}_{t,\perp} \left[|\mathbf{E}|^2 \mathbf{E} \right] + F_2(\bar{q}_m, \bar{\omega}_m) Y, \quad (\text{A43})$$

with $F_1(\bar{q}_m, \bar{\omega}_m) = 1 - |r_1r_2|$ and $\partial_q F_1(\bar{q}_m, \bar{\omega}_m) = -2i|r_1r_2|L$. We introduced the cavity round-trip $\tau_e = 2L_e/v_e$ and the effective cavity length L_e . The latter depends, beyond the standard contribution of the cavity length, upon the penetration length in the DBRs, i.e. $L_e = L + v_e \partial_\omega [(\phi_1 + \phi_2)/2](\bar{\omega}_m)$ while at zeroth order we have

$$F_2(\bar{q}_m, \bar{\omega}_m) \simeq t'_1 (-1)^{n_1} e^{-i\phi_1(\bar{\omega}_m)/2} (1 + |r_2|) \quad (\text{A44})$$

$$\Gamma(\bar{q}_m, \bar{\omega}_m) \simeq (1 + |r_1|)(1 + |r_2|). \quad (\text{A45})$$

The photon decay rate in amplitude is $\kappa = \tau_e^{-1} (1 - |r_1r_2|)/|r_1r_2|$, and we define the coupling parameter $\tilde{h} = F_2(\bar{q}_m, \bar{\omega}_m)/F_1(\bar{q}_m, \bar{\omega}_m)$, which leads us to

$$\left[1 - \frac{i\delta\omega}{\kappa} - \frac{2iL|r_1r_2|}{1-|r_1r_2|} \left(\bar{q}_m \frac{\Delta n}{\bar{n}_m} - \frac{q_\perp^2}{2\bar{q}_m} \right) \right] \mathbf{E} = \tilde{h} Y - \frac{3\bar{\omega}_m \bar{\chi}_3 W}{8i\bar{n}_m c} \frac{(1+|r_1|)(1+|r_2|)}{1-|r_1r_2|} \mathcal{F}_{t,\perp} \left[|\mathbf{E}|^2 \mathbf{E} \right] \quad (\text{A46})$$

By back-transforming to time and transverse space, noting that $\delta\omega = \omega - \omega_0 + \omega_0 - \omega_m$ and that the field is

is a function of $\omega - \omega_0$ we get

$$\frac{1}{\kappa} \frac{\partial \mathbf{E}}{\partial t} = -(1 + i\delta_0) \mathbf{E} + \tilde{h} Y + \frac{i2L|r_1r_2|}{1-|r_1r_2|} \left(\bar{q}_m \frac{\Delta n}{\bar{n}_m} + \frac{\Delta_\perp}{2\bar{q}_m} \right) \mathbf{E} + \frac{3i\bar{\omega}_m \bar{\chi}_3 W}{8\bar{n}_m c} \frac{(1+|r_1|)(1+|r_2|)}{1-|r_1r_2|} |\mathbf{E}|^2 \mathbf{E} \quad (\text{A47})$$

where we defined $\delta_0 = \omega_m - \omega_0$ the detuning at temperature T_0 between the cavity mode and the injection.

The evolution equation for the intra-cavity field given by Eq. A47 is unwieldy as it depends on the DBR transmission t'_1 through the parameter \tilde{h} . However, this dependence can be simplified by a proper scaling of \mathbf{E} . Starting from the output relation Eq. A26 and the expression of L_- given by Eq. A29 we observe, after using the Stokes relations and $l = L/2$ that $O = \alpha \mathbf{E} - Y$ with $\alpha = (-1)^{n_1} e^{-i\phi_1(\bar{\omega}_m)/2} t'_1 / (1 + r_1)$. Setting $E = \alpha \mathbf{E}$ allows for the very simple input-output relation $O = E - Y$. Using that for a resonant DBR $\phi_1(\bar{\omega}_m) = 0$, the coupling with the intra-cavity field $h = \alpha \tilde{h}$ simplifies as

$$h = \frac{(1-|r_1|)(1+|r_2|)}{1-|r_1r_2|} \quad (\text{A48})$$

We further define the cavity enhanced Kerr nonlinearity

(in m^2/V^2)

$$s = \frac{3\bar{\omega}_m \bar{\chi}_3 W}{8\bar{n}_m c} \frac{(1 + |r_2|)(1 + |r_1|)^3}{(1 - |r_1 r_2|) |t_1|^2}, \quad (\text{A49})$$

Normalizing transverse space to the cavity-enhanced diffraction length $l_\perp = \sqrt{\frac{L}{\bar{q}_m} \frac{|r_1 r_2|}{1 - |r_1 r_2|}}$ and time by the photon lifetime κ^{-1} , and introducing the effective detuning taking into account the slow thermal effects through the temperature evolution

$$\delta = \delta_0 - 2\bar{q}_m L \frac{|r_1 r_2|}{1 - |r_1 r_2|} \frac{\partial_T \bar{n}_m}{\bar{n}_m} \delta T \quad (\text{A50})$$

leads us to the equation given in the main text

$$\dot{E} = [i(\Delta_\perp + s|E|^2 - \delta) - 1] E + hY, \quad (\text{A51})$$

We note that $s = +1$ (resp. $s = -1$) corresponds to a focusing (resp. defocusing) Kerr medium while a complex value would take into account two-photon absorption.

Temperature equation We assume that the temperature of the micro-cavity relaxes exponentially towards the equilibrium temperature T_0 set by the Peltier element and at a rate γ . This thermalization is impeded by the presence of a heat source. These ideas materialize as

$$\dot{T} = \gamma(T_0 - T + R_{th}Q), \quad (\text{A52})$$

with R_{th} the thermal impedance in K/W and Q in Watts. The optical power injected into the system that is not re-emitted from both sides of the micro-cavity must be dissipated as heat. This simple statement allows finding that Q is the differences between the norm of Poynting vectors of the injected, reflected and transmitted fields integrated over the surface of the device that we assume to be circular with R , i.e.

$$Q = \pi R^2 \langle \langle \mathcal{E}_i \times \mathcal{H}_i - \mathcal{E}_r \times \mathcal{H}_r - \mathcal{E}_t \times \mathcal{H}_t \rangle \rangle (\text{A53})$$

where the bracket $\langle \cdot \rangle$ represents an average over a few oscillations of the electric field. Assuming no field escapes by the bottom mirror (Gires-Tournois regime $|t_2| \rightarrow 0$), and plane waves so that $\mathcal{H} = \mathcal{E}/\eta$ with $\eta = \sqrt{\mu_0/\epsilon_0} \sim 377 \Omega$ the vacuum impedance we find after simplifications that

$$\dot{\delta} = \gamma [\delta_0 - \delta - \mu_{th} (|Y|^2 - |O|^2)] \quad (\text{A54})$$

with the coupling constant in m^2/V^2

$$\mu_{th} = R_{th} \frac{\pi R^2}{2\eta} 2\bar{q}_m L \frac{|r_1 r_2|}{1 - |r_1 r_2|} \frac{\partial_T \bar{n}_m}{\bar{n}_m} \quad (\text{A55})$$

Interestingly, we notice that our model does not include so far optical absorption in the micro-cavity. Indeed, the term $-E$ in Eq. A51 is not *per se* a loss term since it simply represents the coupling to the external cavity. We can remedy to this problem modifying Eq. A51 with an additional dimensionless loss term α

$$\dot{E} = -(1 + \alpha) E + i(s|E|^2 - \delta) E + hY, \quad (\text{A56})$$

Since thermal effects are slow, we can assume steady states operation in Eq. A56. In that case defining the nonlinear detuning $\theta = \delta - s|E|^2$ we get $E = hY/(1 + \alpha + i\theta)$ and the output $O = E - Y$ in the GTI limit where $h = 2$ reads

$$O = \frac{1 - \alpha - i\theta}{1 + \alpha + i\theta} Y \quad (\text{A57})$$

which corresponds to the intuitive result that the source term in Eq. A54 is proportional to the intracavity field $|Y|^2 - |O|^2 = \alpha |E|^2$. In the limit of small values of α and large μ_{th} , one can neglect α in Eq. A56. We define $\mu_\alpha = \mu_{th}\alpha$ thereby reaching the model given in the main text. Interestingly, we note that introducing nonlinear losses such as two-photon absorption, i.e. $s \in \mathbb{C}$ would induce a dissipation term proportional to the fourth power of the field amplitude.

The last step in our derivation consists in linking the injected field Y to the cavity output O , that is re-injected after one roundtrip upon reflection on the external mirror with amplitude η and phase ϕ , see Fig. 1. This proceeds without difficulty and taking into account the continuous wave injection beam Y_0 we find

$$Y(t) = \eta e^{i\varphi} O(t - \tau) + \sqrt{1 - \eta^2} Y_0 \quad (\text{A58})$$

where we introduced the round-trip phase $\varphi = \omega_0 \tau + \phi$. In absence of transverse effects the final model reads

$$\dot{E} = [i(s|E|^2 - \delta) - 1] E + hY, \quad (\text{A59})$$

$$\dot{\delta} = \gamma (\delta_0 - \delta - \mu_\alpha |E|^2), \quad (\text{A60})$$

$$Y = \eta e^{i\varphi} [E(t - \tau) - Y(t - \tau)] + \sqrt{1 - \eta^2} Y_0. \quad (\text{A61})$$

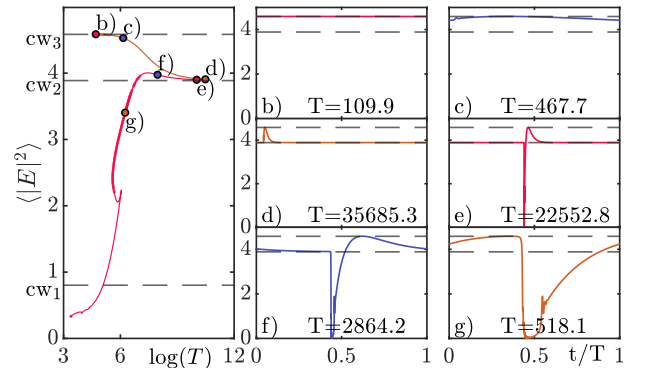


FIG. 11. a) The left Canard region from Fig. 8 on the main text plotted over the period T . On the $\langle |E|^2 \rangle$ -axis one can see three continuous wave plateaus $CW_{1,2,3}$. The branch shows an incomplete homoclinic bifurcation, approaching CW_2 . (b-g) Respective profiles from different marked parts of the branch.

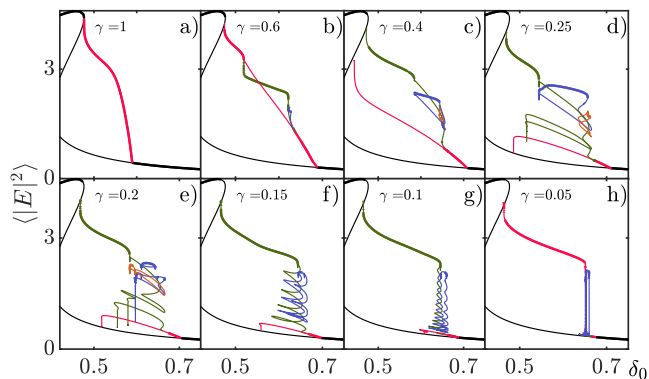


FIG. 12. Emergence of mixed-mode oscillations and a sharp subthreshold to relaxation oscillation transition if a scale separation is introduced. In panels (a) to (h), γ is gradually decrease, leading to a shattering of the periodic branch from (a) (red) towards the bifurcation scenario from Fig. 8, depicted in panel (h). Parameters as in Fig. 8.

Appendix B: Extended bifurcation analysis

Here, we provide additional insight into the complicated bifurcation scenario depicted in Fig. 8 (a). Starting with the bifurcation from the upper continuous wave

(CW) value around iv), we observe a supercritical AH bifurcation, followed by a sharp canard transition. Using numerical path continuation on these solution, yields an interesting phenomenon in the period, seemingly diverging around the middle CW value. Notably, the branch approaches the middle CW value, without reconnecting to it, leading to an incomplete homoclinic bifurcation scenario as indicated in Fig. 11. Here, the relaxation oscillation branch from Fig. 8 (a) is shown with period T as parameter on a logarithmic scale. Different profiles depicted in panels (b-g) indicate how the branch leaves the upper CW in a supercritical AH bifurcation ((b,c)), slowly approaching the middle CW value (d). After a cusp, a spike to zero appears (e), followed by the evolution of relaxation oscillations. In general, the emergence of canard scenarios and mixed-mode oscillations (MMOs) was reported to be a phenomenon resulting from scale separation. Hence, we show an exemplary bifurcation scenario, unveiling the path into scale separation. In Fig. 12 (a), a periodic branch (red) is shown, emerging supercritically from a CW branch (black). The parameters are the same as in Fig. 8, except for the choice of $\gamma = 1$. Reducing γ leads to the emergence of a second periodic branch in a period doubling bifurcation, as well as additional small branches, which are the MMOs. As we further reduce γ , the scenario becomes more complex, while also getting confined to a decreasing parameter regime. Finally, in Fig. 12 (h), we recover the scenario presented in Fig. 8.

-
- [1] A. Winfree, *The Geometry of Biological Time*, Biomathematics (Berlin) (Springer Verlag, 1980).
- [2] E. Meron, Pattern formation in excitable media, *Physics Reports* **218**, 1 (1992).
- [3] E. M. Izhikevich, *Dynamical systems in neuroscience : the geometry of excitability and bursting*, Computational neuroscience (MIT Press, Cambridge, Mass., London, 2007).
- [4] A. S. Mikhailov and K. Showalter, Control of waves, patterns and turbulence in chemical systems, *Physics Reports* **425**, 79 (2006).
- [5] A. Mikhailov, *Foundations of Synergetics I: Distributed Active Systems*, Springer Series in Synergetics (Springer Berlin Heidelberg, 2012).
- [6] E. M. Izhikevich, Neural excitability, spiking and bursting, *Int. J. Bifurc. Chaos Appl. Sci. Eng.* **10**, 1171 (2000).
- [7] L. Kuhnert, K. Agladze, and V. Krinsky, Image processing using light-sensitive chemical waves, *Nature* **337**, 244 (1989).
- [8] P. R. Prucnal, B. J. Shastri, T. F. de Lima, M. A. Nahmias, and A. N. Tait, Recent progress in semiconductor excitable lasers for photonic spike processing, *Adv. Opt. Photonics* **8**, 228 (2016).
- [9] B. Braeckeveldt, K. J. H. Peters, B. Verdonschot, B. Maes, and S. R. K. Rodriguez, Memory-induced excitability in optical cavities, *Phys. Rev. Res.* **6**, 023008 (2024).
- [10] J. M. Davidenko, A. V. Pertsov, R. Salomonsz, W. Baxter, and J. Jalife, Stationary and drifting spiral waves of excitation in isolated cardiac muscle, *Nature* **355**, 349 (1992).
- [11] Z. Qu, G. Hu, A. Garfinkel, and J. N. Weiss, Nonlinear and stochastic dynamics in the heart, *Phys. Rep.* **543**, 61 (2014).
- [12] Dynamics of nearly inviscid Faraday waves in almost circular containers, *Phys. D: Nonlinear Phenom.* **201**, 83 (2005).
- [13] M. Higuera, J. Porter, and E. Knobloch, Faraday waves, streaming flow, and relaxation oscillations in nearly circular containers, *Chaos* **18**, 10.1063/1.2779860 (2008).
- [14] F. Plaza, M. Velarde, F. Arecchi, S. Boccaletti, M. Ciofini, and R. Meucci, Excitability following an avalanche-collapse process, *Europhys. Lett.* **38**, 85 (1997).
- [15] G. Ansmann, R. Karnatak, K. Lehnertz, and U. Feudel, Extreme events in excitable systems and mechanisms of their generation, *Phys. Rev. E* **88**, 052911 (2013).
- [16] P. Couillet, T. Frisch, J. Gilli, and S. Rica, Excitability in liquid crystal, *Chaos* **4**, 485 (1994).
- [17] T. Piwonski, J. Houlihan, T. Busch, and G. Huyet, Delay-induced excitability, *Phys. Rev. Lett.* **95**, 040601 (2005).
- [18] F. Gires and P. Tournois, Interferometre utilisable pour la compression d'impulsions lumineuses modulees en frequence, *C. R. Acad. Sci. Paris*, 6112 (1964).
- [19] C. Schelte, A. Pimenov, A. G. Vladimirov, J. Javaloyes, and S. V. Gurevich, Tunable Kerr frequency combs and temporal localized states in time-delayed Gires-Tournois interferometers, *Opt. Lett.* **44**, 4925 (2019).

- [20] T. G. Seidel, J. Javaloyes, and S. V. Gurevich, A normal form for frequency combs and localized states in Kerr–Gires–Tournois interferometers, *Opt. Lett.* **47**, 2979 (2022).
- [21] T. G. Seidel, S. V. Gurevich, and J. Javaloyes, Conservative solitons and reversibility in time delayed systems, *Phys. Rev. Lett.* **128**, 083901 (2022).
- [22] E. R. Koch, T. G. Seidel, S. V. Gurevich, and J. Javaloyes, Square-wave generation in vertical external-cavity Kerr–Gires–Tournois interferometers, *Opt. Lett.* **47**, 4343 (2022).
- [23] M. Stöhr, E. R. Koch, J. Javaloyes, S. V. Gurevich, and M. Wolfrum, Square waves and Bykov T-points in a delay algebraic model for the Kerr–Gires–Tournois interferometer, *Chaos* **33**, 10.1063/5.0173320 (2023).
- [24] R. Straube, D. Flockerzi, S. C. Müller, and M. J. Hauser, Origin of bursting pH oscillations in an enzyme model reaction system, *Phys. Rev. E* **72**, 066205 (2005).
- [25] F. Marino and F. Marin, Coexisting attractors and chaotic canard explosions in a slow-fast optomechanical system, *Phys. Rev. E* **87**, 052906 (2013).
- [26] Y. Zheng and L. Bao, Time-delay effects on mixed-mode oscillations of modified chua’s system, *Nonlinear Dyn.* **80**, 1521 (2015).
- [27] M. Giudici, C. Green, G. Giacomelli, U. Nespolo, and J. Tredicce, Andronov bifurcation and excitability in semiconductor lasers with optical feedback, *Phys. Rev. E* **55**, 6414 (1997).
- [28] M. C. Eguia and G. B. Mindlin, Semiconductor laser with optical feedback: From excitable to deterministic low-frequency fluctuations, *Phys. Rev. E* **60**, 1551 (1999).
- [29] H. Wünsche, O. Brox, M. Radziunas, and F. Henneberger, Excitability of a semiconductor laser by a two-mode homoclinic bifurcation, *Phys. Rev. Lett.* **88**, 023901 (2001).
- [30] O. D’Huys, R. Veltz, A. Dolcemascolo, F. Marino, and S. Barland, Canard resonance: On noise-induced ordering of trajectories in heterogeneous networks of slow-fast systems, *J. Phys. Photonics* **3**, 024010 (2021).
- [31] P. Coullet, D. Daboussy, and J. Tredicce, Optical excitable waves, *Phys. Rev. E* **58**, 5347 (1998).
- [32] F. Marino and S. Balle, Excitable optical waves in semiconductor microcavities, *Phys. Rev. Lett.* **94**, 094101 (2005).
- [33] S. Wieczorek, B. Krauskopf, T. B. Simpson, and D. Lenstra, The dynamical complexity of optically injected semiconductor lasers, *Phys. Rep.* **416**, 1 (2005).
- [34] S. Barbay, R. Kuszelewicz, and A. M. Yacomotti, Excitability in a semiconductor laser with saturable absorber, *Opt. Lett.* **36**, 4476 (2011).
- [35] F. Selmi, R. Braive, G. Beaudoin, I. Sagnes, R. Kuszelewicz, and S. Barbay, Relative refractory period in an excitable semiconductor laser, *Phys. Rev. Lett.* **112**, 183902 (2014).
- [36] F. Marino, M. De Rosa, and F. Marin, Canard orbits in Fabry-Perot cavities induced by radiation pressure and photothermal effects, *Phys. Rev. E* **73**, 026217 (2006).
- [37] J. Javaloyes and S. Balle, Influence of thermal effects on cross-gain modulation characteristics in VCSCOA, *IEEE J. Quantum Electron.* **43**, 65 (2007).
- [38] S. Beri, L. Mashall, L. Gelens, G. Van der Sande, G. Mezosi, M. Sorel, J. Danckaert, and G. Verschaffel, Excitability in optical systems close to Z_2 -symmetry, *Phys. Lett. A* **374**, 739 (2010).
- [39] R. Otupiri, B. Garbin, N. G. R. Broderick, and B. Krauskopf, Excitability in an all-fiber laser with a saturable absorber section, *J. Opt. Soc. Am. A* **38**, 1695 (2021).
- [40] S. Barland, O. Piro, M. Giudici, J. R. Tredicce, and S. Balle, Experimental evidence of van der Pol–Fitzhugh–Nagumo dynamics in semiconductor optical amplifiers, *Phys. Rev. E* **68**, 036209 (2003).
- [41] F. Marino, G. Catalán, P. Sánchez, S. Balle, and O. Piro, Thermo-optical “canard orbits” and excitable limit cycles, *Phys. Rev. Lett.* **92**, 073901 (2004).
- [42] E. Shchepakina and O. Korotkova, Condition for canard explosion in a semiconductor optical amplifier, *J. Opt. Soc. Am. B* **28**, 1988 (2011).
- [43] T. E. Drake, J. R. Stone, T. C. Briles, and S. B. Papp, Thermal decoherence and laser cooling of Kerr microresonator solitons, *Nat. Photonics* **14**, 480 (2020).
- [44] I. Ortega-Piwonka, O. Piro, J. Figueiredo, B. Romeira, and J. Javaloyes, Bursting and excitability in neuromorphic resonant tunneling diodes, *Phys. Rev. Applied* **15**, 034017 (2021).
- [45] R. FitzHugh, Impulses and physiological states in theoretical models of nerve membrane, *Biophys. J.* **1**, 445 (1961).
- [46] I. Nagumo, S. Arimoto, and S. Yoshizawa, An active pulse transmission line simulating nerve axon, *Proceedings of the IRE* **50**, 2061 (1962).
- [47] F. Marino, F. Marin, S. Balle, and O. Piro, Chaotically spiking canards in an excitable system with 2D inertial fast manifolds, *Phys. Rev. Lett.* **98**, 074104 (2007).
- [48] V. A. Makarov, V. I. Nekorkin, and M. G. Velarde, Spiking behavior in a noise-driven system combining oscillatory and excitatory properties, *Phys. Rev. Lett.* **86**, 3431 (2001).
- [49] F. G. Della Corte, G. Cocorullo, M. Iodice, and I. Rendina, Temperature dependence of the thermo-optic coefficient of Inp, GaAs, and SiC from room temperature to 600 K at the wavelength of $1.5\mu\text{m}$, *Appl. Phys. Lett.* **77**, 1614 (2000).
- [50] S.-G. Lee, A. Neiman, and S. Kim, Coherence resonance in a Hodgkin-Huxley neuron, *Phys. Rev. E* **57**, 3292 (1998).
- [51] K. Al-Naimee, F. Marino, M. Ciszak, R. Meucci, and F. T. Arecchi, Chaotic spiking and incomplete homoclinic scenarios in semiconductor lasers with optoelectronic feedback, *New J. Phys.* **11**, 073022 (2009).